Topological triply-degenerate point with double Fermi arcs

Yihao Yang[1,2,#], Hong-xiang Sun[3,#], Jian-ping Xia[3], Haoran Xue[1,2], Zhen Gao[1,2], Yong Ge[3], Ding Jia[3], Shou-qi Yuan[3], Yidong Chong[1,2,], and Baile Zhang[1,2,*]*

[1]Division of Physics and Applied Physics, School of Physical and Mathematical Sciences, Nanyang Technological University, 21 Nanyang Link, Singapore 637371, Singapore.

[2]Centre for Disruptive Photonic Technologies, The Photonics Institute, Nanyang Technological University, 50 Nanyang Avenue, Singapore 639798, Singapore.

[3]Research Center of Fluid Machinery Engineering and Technology, Faculty of Science, Jiangsu University, Zhenjiang 212013, China.

#These authors contributed equally to this work.

*Correspondence to: (Y. C.) yidong@ntu.edu.sg; (B. Z.) blzhang@ntu.edu.sg.

ABSTRACT

Unconventional chiral particles have recently been predicted to appear in certain three dimensional (3D) crystal structures containing three- or more-fold linear band degeneracy points (BDPs)[1-4]. These BDPs carry topological charges, but are distinct from the standard twofold Weyl points or fourfold Dirac points, and cannot be described in terms of an emergent relativistic field theory[1]. Here, we report on the experimental observation of a topological threefold BDP in a 3D phononic crystal. Using direct acoustic field mapping, we demonstrate the existence of the threefold BDP in the bulk bandstructure, as well as doubled Fermi arcs of surface states consistent with a topological charge of 2. Another novel BDP, similar to a Dirac point but carrying nonzero topological charge, is connected to the threefold BDP via the doubled Fermi arcs. The Fermi arcs form double helicoids spanning a broad frequency range (relative bandwidth >25%). We show that the non-contractibility of these arcs gives rise to the phenomenon of topologically protected negative refraction of surface states on all surfaces of the sample. Our findings pave the way to using these unconventional particles for exploring new emergent physical phenomena, and may find applications in symmetry-stabilized 3D zero-index metamaterials.

It is a remarkable fact that particle-like excitations described by relativistic field theories can arise in non-relativistic periodic media whose bandstructures contain linear band degeneracy points (BDPs). For example, two-dimensional (2D) hexagonal crystals like graphene can exhibit stable twofold linear BDPs, called Dirac points, whose excitations act as 2D massless spin-1/2 Dirac particles[5]. In three dimensions

(3D), the analogous twofold linear BDPs are called Weyl points, and their excitations are massless particles of a type hypothesized but so far not known to exist in high-energy particle physics, i.e., spin-1/2 Weyl particles[6-14]. Weyl points carry topological charges (Chern numbers) of either +1 or -1[6-14], corresponding to the chirality (left- or right-handed) of the Weyl particles. As a result, each pair of oppositely charged Weyl points, when projected on a surface, is joined by an unclosed arc, called a Fermi arc, of topologically-protected surface states. A 3D Dirac point, on the other hand, is a fourfold BDP that can be viewed as two overlapping Weyl points with opposite topological charges; it carries no net topological charge and thus lacks topological surface states[12,15]. Weyl and Dirac particles obey the Lorentz group of free-space relativistic transformations, and can be regarded as emergent relativistic particles with the group velocity of the linear BDP playing the role of the speed of light.

Recently, it has been predicted that certain bandstructures can have symmetry-stabilized linear BDPs that host a family of unconventional chiral quasiparticles beyond Weyl and Dirac particles[1-4]. These "unconventional BDPs" occur in nonsymmorphic crystal structures and carry nonzero topological charge[1]. One such candidate is a threefold linear BDP (henceforth called the "triple point") carrying topological charge 2. This is qualitatively distinct from twofold BDPs generated by merging a pair of Weyl points of the same charge, which have quadratic or higher-order dispersion relations[16-18]. The excitations of the triple point behave as spin-1 quasiparticles[19], unlike Weyl and Dirac particles which are spin-1/2. Because the triple point has a topological charge of 2, there are two topologically-protected Fermi arcs emanating simultaneously from its projection onto a 2D surface. This topological charge distinguishes the present triple point from recently-observed threefold BDPs in MoP and WC crystals[20,21], which do not carry topological charge, similar to 3D Dirac points. A threefold degeneracy has also been observed in the phonon spectrum of FeSi[22], but at zero frequency, which is not a BDP in the sense considered in Ref. [1]. To our knowledge, the double Fermi arcs predicted to occur for topologically nontrivial threefold BDPs[1] has never been observed.

We have designed and implemented an acoustic metamaterial – a classical 3D phononic crystal with a nonsymmorphic structure – featuring a charge-2 triple point. By direct field-mapping, we demonstrate experimentally that the three affected acoustic bands have the desired dispersion characteristics at the center of the Brillouin zone (Γ). Another interesting bandstructure feature observed in these measurements is a charge-2 fourfold BDP (henceforth called the "quadruple point") existing at the corner of the Brillouin zone. It is equivalent to a pair of Weyl points with the *same* topological charge, unlike standard 3D Dirac points which are equivalent to a pair of oppositely-charged Weyl points (thus carrying zero topological charge). Moreover, we are able to verify the topological charges of both BDPs by imaging the hallmark "double Fermi arcs" that extend from the triple point to the quadruple point. These double Fermi arcs form double

helicoids over a broad frequency range (relative bandwidth >25%), and are thus experimentally very robust. We show that the Fermi arc surface states exhibit the distinctive phenomenon of topologically protected negative refraction when propagating across corners of the sample.

The sample of 3D phononic crystal, shown in Figs. 1a-b, consists of 20×20×10 unit cells in a cubic lattice structure, with the noncentrosymmetric space group $P2_13$ (No. 198) (see Supplementary Information for symmetry analysis and effective Hamiltonian descriptions). The lattice constant is a=20 mm. As shown in Fig.1c, each unit cell contains four junctions, at (u, u, u), (0.5a+u, 0.5a-u, -u), (-u, 0.5a+u, 0.5a-u), and (0.5a-u, -u, 0.5a+u), where u=0.1a. Each junction connects to 6 neighbouring junctions via solid rods of radius r=0.14a; the rest of the volume is filled with air. The resulting crystal structure has three twofold screw symmetries, along each <100> axis, and a C_3 rotational symmetry along the <111> axes. The sample is fabricated from photosensitive resin via 3D printing, and is self-supporting.

The bandstructure for acoustic (sound) waves in this lattice was calculated numerically, and the results are shown in Figs. 1d-f. There exists a triple point at the Γ point in the center of the Brillouin zone, and a quadruple point at the R point in the corner of the Brillouin zone. The triple point can be described by a three-band effective Hamiltonian $H_3(k) \sim k \cdot L$, where k is the wavevector and L is the spin-1 matrix representation of the rotation generator[1-4], and the Chern numbers of the bands are +2, 0, and -2, respectively. As for the quadruple point, it can be treated as a direct sum of two identical Weyl points, via the four-band effective Hamiltonian $H_4(k) \sim \begin{pmatrix} k.\sigma & 0 \\ 0 & k.\sigma \end{pmatrix}$, where σ denotes the Pauli matrices[2-4]; the bands have Chern numbers of +2 and -2, respectively. All Chern numbers were calculated numerically from the acoustic Bloch wavefunctions using the Wilson loop method[23] (see Supplementary Information for details). The two BDPs have opposite topological charges ±2 that sum to zero, consistent with the Nielsen-Ninomiya theorem[24]. Note that although the BDPs occur at different frequencies, there are no trivial bands occupying the frequency range between them. Therefore, this phononic crystal provides an extremely "clean" platform for studying the physical effects of the BDPs.

We determine the bulk bandstructure experimentally by threading acoustic sources and probes through the air holes of the phononic structure and measuring the pressure field distribution along a horizontal plane in the middle of the sample, with a source fixed 4 cm below the plane (Fig. 2a). After performing a 2D Fourier transform, we obtain the projected band structure (projected from 3D into the 2D plane) shown in Fig. 2b. The results reveal, as expected, (i) a nodal point (the triple point) at 13.4 kHz projected onto $\bar{\Gamma}$ in the 2D Brillouin zone, and (ii) another nodal point (the quadruple point) at 11.2 kHz projected onto $\bar{M}$. This is in excellent quantitative agreement with the numerically-calculated projected bandstructure shown in Fig. 2c.

Next, we use surface measurements to verify the topological charges of the BDPs. The setup for the surface measurements is shown in Fig. 3a. The phononic crystal is placed on an acrylic board that behaves as a hard boundary for sound. A source is placed at the center of the bottom surface, exciting acoustic surface waves. We then insert a probe into the sample from the top, and measure the acoustic field distribution just above the surface. After applying a 2D Fourier transform, we obtain the surface spectrum shown in Figs. 3b, d, and f, which agree very well with the numerically-calculated surface dispersion (Figs. 3c, e, and g). It is evident from the measurement results that there exist two Fermi arcs, consistent with the predicted topological charges of the BDPs. Over frequencies ranging from 10.3 kHz to 13.6 kHz, the dispersion surface forms a double helicoid: two surface sheets winding around the triple and quadruple points (see Supplementary Information for frequencies at 13.3 and 13.6 kHz, whose Fermi arcs have a shape similar to that at 13 kHz in Fig. 3g). Note that the back turns at 12.7 kHz and 13 kHz in Fig. 3f and some extra features at 10.3 kHz in Fig. 3d are induced by the bulk dispersion. The isofrequency curve forms a single non-contractible loop (Figs. 3d and f) wrapping around the torus of Brillouin zone, which is qualitatively different from those of trivial surface states (whose isofrequency curves are closed loops which can deform into an even number of non-contractible loops), and also different from the non-trivial surface states of conventional Weyl points (whose dispersion surfaces are single helicoids, and isofrequency curves are open arcs)[2].

Note that the previously observed charge-0 triply-degenerate point[20] can also support multiple Fermi arcs[21], but those Fermi arcs are contractible and not topologically protected in general[15]. Here we demonstrate that the topologically protected non-contractible Fermi arc surface states in our system give rise to a distinctive physical phenomenon: topologically-protected negative surface refraction across two surfaces of the sample. As shown in Figs. 4a-b, the adjacent surfaces are covered with acrylic boards (see the schematic illustration in Supplementary Information), a source is fixed on one surface, and the field distribution is measured along both surfaces. When the surface states impinge the edge between the two surfaces, no reflection occurs, due to the lack of a reflection channel. The refracted wave on the other surface lies on the same side of the normal as the incident wave, a phenomenon referred to as "negative refraction" for topological surface waves[25]. This can be explained from the isofrequency contour of the surface states. Because the topological triple point and quadruple point are at Γ and R, when projected to the surfaces of a cubic sample they generate identical Fermi arcs in each surface (up to a 90° rotation). It can be seen in Fig. 4c that the isofrequency contours on the two surfaces are simply rotated by 90° relative to each other, resulting in negative refraction. Note that only with k_z in the range from $0.3\pi/a$ to $0.8\pi/a$ can reflectionless negative refraction occur. In our experiments, we optimized the excitation of the surface states to let their momenta mainly locate in this range (see details in Supplementary Information). The 90° rotation of isofrequency contours is applicable to all six surfaces of the sample, so the negative refraction

phenomenon can occur at all twelve edges. Such *all-surface* topological negative refraction is unachievable in previously demonstrated system[25].

Our work thus experimentally demonstrates two novel types of topologically nontrivial linear BDPs, a charge-2 triple point and a charge-2 quadruple point, that lie outside the pre-existing Weyl/Dirac types. Due to the ease with which phononic crystals can be fabricated and analysed, it will be interesting to use them to look for other types of unconventional BDPs, which are stabilized by different choices of crystal symmetry and can carry topological charges higher than ±2, and thus more intricate surface state dispersions. It can also be envisioned that exotic chiral Landau levels may arise from these unconventional topological BDPs compared to the conventional Weyl points[26,27]. In terms of acoustic applications, the extremely wide bandwidth of topological surface states and all-surface negative refraction show promising use in defect-tolerate waveguiding and acoustic manipulation. As the triple point lies at the center of the Brillouin zone, it may be interpretable in terms of a 3D zero-index metamaterial[28] – but which, unlike previously-studied zero-index metamaterials based on fine-tuned accidental degeneracies[29], is symmetry-stabilized and thus extremely robust, with potentially interesting implications for 3D acoustic or electromagnetic wavefront tailoring.

Note added: After our submission, we were notified of several independent works reporting double Fermi arcs in fermionic systems[30-33].

Acknowledgments

We thank H. S. Tan at Nanyang Technological University for helpful discussions. This work was sponsored by Singapore Ministry of Education under Grants No. MOE2018-T2-1-022 (S), MOE2015-T2-1-070, MOE2015-T2-2-008, MOE2016-T3-1-006 and Tier 1 RG174/16 (S). H.S. acknowledges the support of the National Natural Science Foundation of China (11774137).

Authors Contributions

All authors contributed extensively to this work. Y.Y. designed the phononic crystal and performed the simulations. Y.Y., H.X., Z.G., S.Y. and H.S. fabricated the sample and designed the experiments. H.S., J.X., Y.G. and D.J. performed measurements. Y.Y., Y.C. and B.Z. analyzed data and wrote the paper. Y.C. and B.Z. supervised the project.

Competing Financial Interests

The authors declare no competing financial interests.

Data availability

The data that support the findings of this study are available from the corresponding author upon reasonable request.

References

1 Bradlyn, B. *et al.* Beyond Dirac and Weyl fermions: Unconventional quasiparticles in conventional crystals. *Science* **353**, aaf5037 (2016).

2 Zhang, T. *et al.* Double-weyl phonons in transition-metal monosilicides. *Phys. Rev. Lett.* **120**, 016401 (2018).

3 Chang, G. *et al.* Unconventional chiral Fermions and large topological Fermi arcs in RhSi. *Phys. Rev. Lett.* **119**, 206401 (2017).

4 Tang, P., Zhou, Q. & Zhang, S.-C. Multiple types of topological fermions in transition metal silicides. *Phys. Rev. Lett.* **119**, 206402 (2017).

5 Novoselov, K. S. *et al.* Two-dimensional gas of massless Dirac fermions in graphene. *Nature* **438**, 197-200 (2005).

6 Wan, X., Turner, A. M., Vishwanath, A. & Savrasov, S. Y. Topological semimetal and Fermi-arc surface states in the electronic structure of pyrochlore iridates. *Phys. Rev. B* **83**, 205101 (2011).

7 Xu, S.-Y. *et al.* Discovery of a Weyl fermion semimetal and topological Fermi arcs. *Science* **349**, 613-617 (2015).

8 Lu, L. *et al.* Experimental observation of Weyl points. *Science* **349**, 622-624 (2015).

9 Lv, B. *et al.* Experimental discovery of Weyl semimetal TaAs. *Phys. Rev. X* **5**, 031013 (2015).

10 Xiao, M., Chen, W.-J., He, W.-Y. & Chan, C. T. Synthetic gauge flux and Weyl points in acoustic systems. *Nat. Phys.* **11**, 920-924 (2015).

11 Noh, J. *et al.* Experimental observation of optical Weyl points and Fermi arc-like surface states. *Nat. Phys.* **13**, 611-617 (2017).

12 Armitage, N., Mele, E. & Vishwanath, A. Weyl and Dirac semimetals in three-dimensional solids. *Rev. Mod. Phys.* **90**, 015001 (2018).

13 Yang, B. *et al.* Ideal Weyl points and helicoid surface states in artificial photonic crystal structures. *Science* **359**, 1013-1016 (2018).

14 Li, F., Huang, X., Lu, J., Ma, J. & Liu, Z. Weyl points and Fermi arcs in a chiral phononic crystal. *Nat. Phys.* **14**, 30-34 (2018).

15 Kargarian, M., Randeria, M. & Lu, Y.-M. Are the surface Fermi arcs in Dirac semimetals topologically protected? *Proc. Natl. Acad. Sci.* **113**, 8648-8652 (2016).

16 Fang, C., Gilbert, M. J., Dai, X. & Bernevig, B. A. Multi-Weyl topological semimetals stabilized by point group symmetry. *Phys. Rev. Lett.* **108**, 266802 (2012).

17 Huang, S.-M. *et al.* New type of Weyl semimetal with quadratic double Weyl fermions. *Proc. Natl. Acad. Sci.* **113**, 1180-1185 (2016).

18 Chen, W. J., Xiao, M. & Chan, C. T. Photonic crystals possessing multiple Weyl points and the experimental observation of robust surface states. *Nat. Commun.* **7**, 13038 (2016).
19 Manes, J. L. Existence of bulk chiral fermions and crystal symmetry. *Phys. Rev. B* **85**, 155118 (2012).
20 Lv, B. *et al.* Observation of three-component fermions in the topological semimetal molybdenum phosphide. *Nature* **546**, 627-631 (2017).
21 Ma, J.-Z. *et al.* Three-component fermions with surface Fermi arcs in tungsten carbide. *Nat. Phys.* **14**, 349-354 (2018).
22 Miao, H. *et al.* Observation of double Weyl phonons in parity-breaking FeSi. *Phys. Rev. Lett.* **121**, 035302 (2018).
23 Yu, R., Qi, X. L., Bernevig, A., Fang, Z. & Dai, X. Equivalent expression of Z2 topological invariant for band insulators using the non-Abelian Berry connection. *Phys. Rev. B* **84**, 075119 (2011).
24 Nielsen, H. B. & Ninomiya, M. A no-go theorem for regularizing chiral fermions. *Phys. Lett. B* **105**, 219-223 (1981).
25 He, H. *et al.* Topological negative refraction of surface acoustic waves in a Weyl phononic crystal. *Nature* **560**, 61-64 (2018).
26 Jia, H. *et al.* Observation of chiral zero mode in inhomogeneous three-dimensional Weyl metamaterials. *Science* **363**, 148-151 (2019).
27 Peri, V., Serra-Garcia, M., Ilan, R. & Huber, S. D. Axial-field-induced chiral channels in an acoustic Weyl system. *Nat. Phys.*, 1 (2019).
28 Saba, M., Hamm, J. M., Baumberg, J. J. & Hess, O. Group theoretical route to deterministic weyl points in chiral photonic lattices. *Phys. Rev. Lett.* **119**, 227401 (2017).
29 Huang, X., Lai, Y., Hang, Z. H., Zheng, H. & Chan, C. Dirac cones induced by accidental degeneracy in photonic crystals and zero-refractive-index materials. *Nat. Mater.* **10**, 582-586 (2011).
30 Sanchez, D. S. *et al.* Discovery of topological chiral crystals with helicoid arc states. *arXiv preprint arXiv:1812.04466* (2018).
31 Schröter, N. *et al.* Topological semimetal in a chiral crystal with large chern numbers, multifold band crossings, and long Fermi-arcs. *arXiv preprint arXiv:1812.03310* (2018).
32 Rao, Z.-C. *et al.* New classes of chiral topological nodes with non-contractible surface Fermi arcs in CoSi. *arXiv preprint arXiv:1901.03358* (2019).
33 Takane, D. *et al.* Observation of Chiral Fermions with a Large Topological Charge and Associated Fermi-Arc Surface States in CoSi. *Phys. Rev. Lett.* **122**, 076402 (2019).

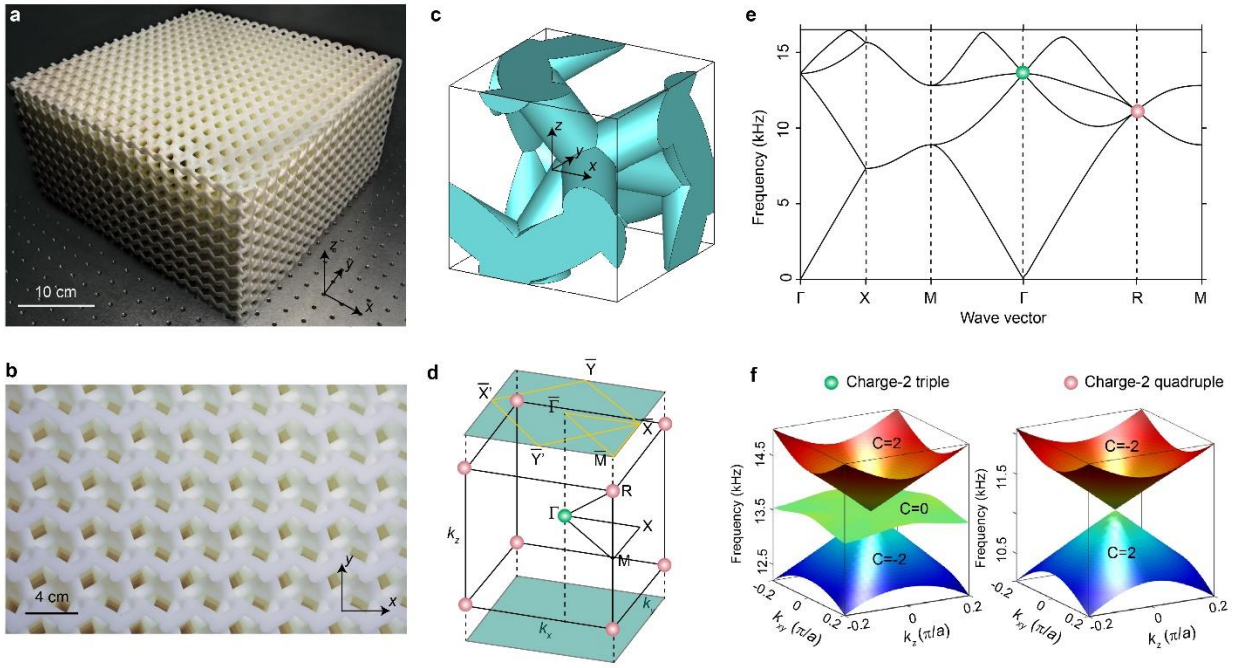

Figure 1. 3D phononic crystal with a charge-2 triple point and a charge-2 quadruple point. (a-b) Photographs of the fabricated sample. (c) Unit cell of the phononic crystal. (d-e) Brillouin zone and band structure of the phononic crystal, with red and green points indicating the triple point and quadruple point, respectively. (f) 2D band structures in the vicinity of the triple point and quadruple points. The Chern number of each band is labeled.

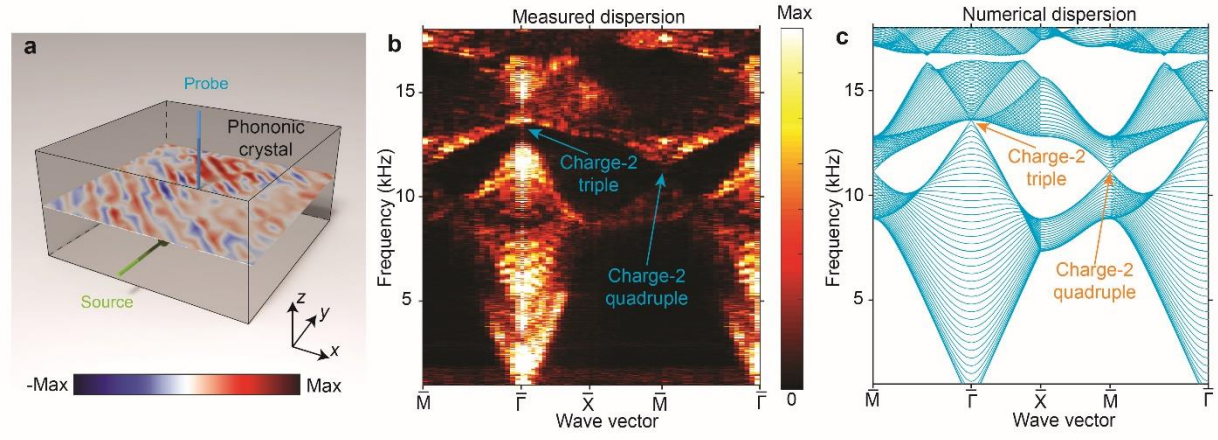

Figure 2. Experimental observation of a charge-2 triple point and a charge-2 quadruple point. (a) Experimental setup. The field distributions are measured along the middle plane of the sample. (b) Measured projected band spectrum. The colour bar indicates the energy intensity. (c) Numerically-calculated projected band spectrum.

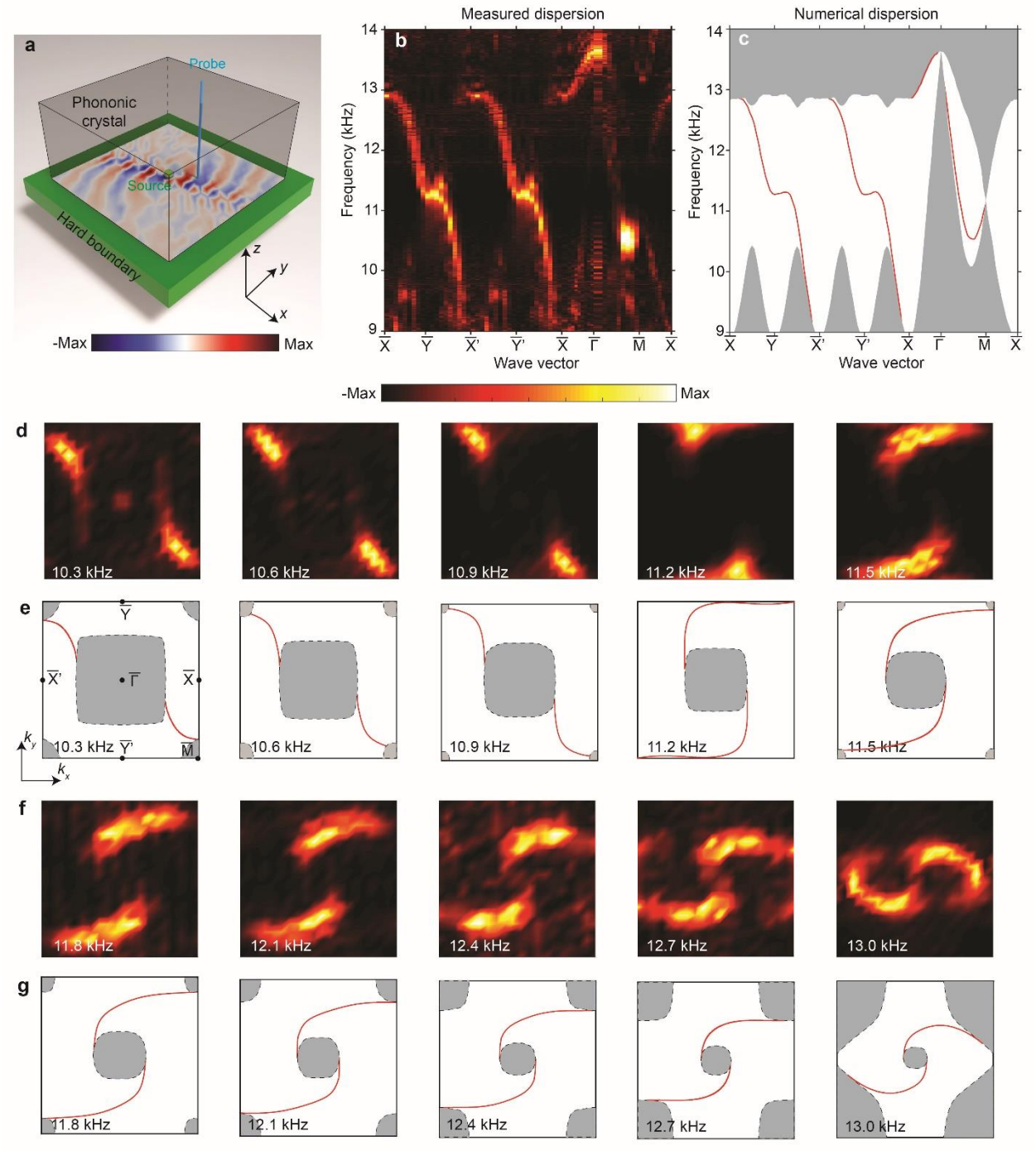

Figure 3. Experimental observation of the double-helicoid topological surface states. (a) Experimental setup. The field distributions are measured along the bottom surface of the sample. The sample sits on an acrylic board that acts as a hard boundary for sound. (b) Measured surface dispersion of the phononic crystal along the high-symmetry lines. (c) Numerical surface dispersion of the phononic crystal along the high-symmetry lines. (d and f) Measured surface isofrequency contours from 10.3 kHz to 13.0 kHz. (e and g) Numerically-calculated surface isofrequency contours from 10.3 kHz to 13.0 kHz. The grey regions and

the red lines represent the projected bulk dispersions and surface dispersions, respectively. The plotted range for each panel is $[-\pi/a, \pi/a]^2$. The colour bar below (b) shows the energy intensity.

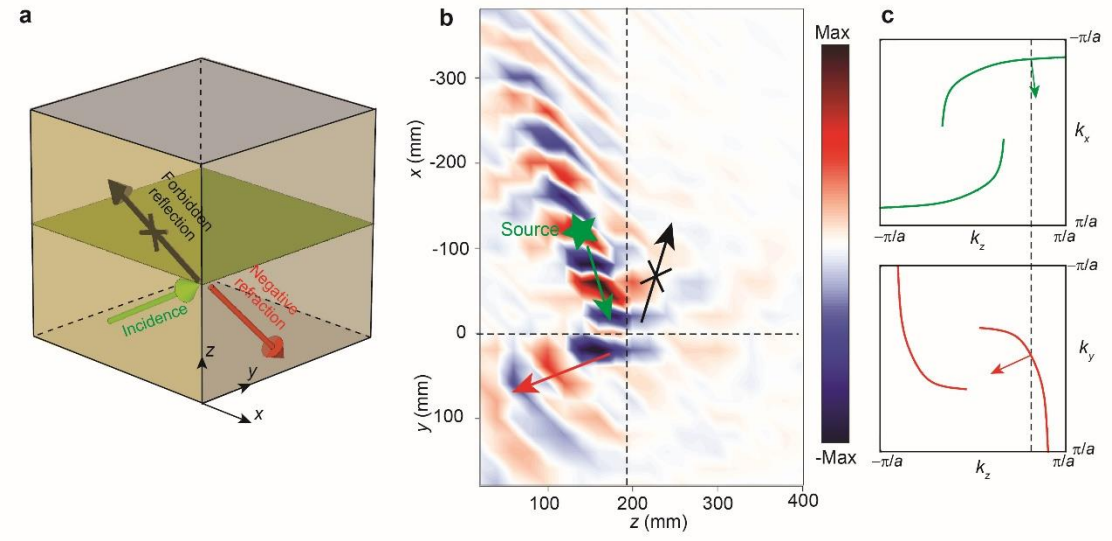

Figure 4. Negative refraction of topological surface states. (a) Schematic of the negative refraction experiment. The green, black, and red arrows represent incidence, reflection, and refraction respectively. The green plane denotes the normal. (b) Measured surface acoustic waves on the y=0 mm and x=0 mm planes at 11.8 kHz. The color bar measures the sound pressure. (c) Isofrequency contours for the surface states on the y=0 mm and x=0 mm planes, respectively. The arrows represent the directions of the group velocity that are normal to the isofrequency contours.

Methods

Numerical simulation. All simulations are performed using the COMSOL Multiphysics software package. Due to the large difference between the impedance of air and that of the photosensitive resin, the photosensitive resin boundaries are treated as hard boundaries. The air density and speed of sound are 1.18 kg/m^3 and 343 m/s, respectively. To calculate the bulk dispersion of the unit cell, periodic boundary conditions are applied in all three spatial directions. To calculate the surface wave modes, periodic boundary conditions are imposed in the x and y directions, with hard boundaries in the z direction. As the surface wave modes are highly confined at the surface, it is sufficient to have 10 unit cells in the z direction.

Experiment. The sample is fabricated with an additive manufacturing technique, i.e., stereo lithography. The material is photosensitive resin with modulus 2880 MPa and density 1.10 g/cm^3. To experimentally excite the surface states, a broadband sound signal is launched by a balanced armature speaker (radius of about 1.0 mm) driven by a power amplifier, and is placed at the center of the bottom surface of the sample. For the bulk states, a broadband sound signal is launched from a narrow tube (radius of about 1.5 mm, length of about 10 cm) that penetrates through one side of the sample. The distance between the tube tip and the measured plane is about 20 mm. The acoustic pressure fields are measured with two microphones (radius of about 3.2 mm, Brüel&Kjær Type 4961), each of which is placed in a sealed sleeve with a tube (radius of 1.0 mm, length of 20 cm) that penetrates into the sample. As the tubes are much smaller than the air holes (approximately 7 mm×7 mm area), the tubes have negligible influence on the measured sound field, as verified in the measured field patterns in Fig. 2(a), Fig. 3(a), and Fig. 4(b). In the measurements, one microphone is moved to scan the 3D acoustic field point by point, and the other microphone is fixed near the sound source to provide the reference signal. The scanning steps in the x and y directions are both 20.0 mm. The amplitude and phase of acoustic pressure field are recorded and the corresponding spectrum is resolved by Brüel&Kjær 3160-A-022 module. Note that due to the non-resonant nature of the designed structure, the acoustic waves experience negligible losses. To obtain the dispersions of both bulk (Fig. 2(b)) and surface states (Fig. 3(b), (d), and (f)), Fourier transform are applied to the measured complex field patterns.